Check for updates

ADVANCING EARTH AND SPACE SCIENCES

JGR Biogeosciences

RESEARCH ARTICLE
10.1029/2025JG008765

Shrub Mangroves Facilitate Self-Sustaining Conditions for Colonization: Insights From the Nanliu Delta, China

Xiaoyan Zhou[1,2], Zhijun Dai[1], Davide Tognin[2], Jiejun Luo[1], Riming Wang[3], Bingbin Feng[3], and Luca Carniello[2]

[1]State Key Laboratory of Estuarine and Coastal Research, East China Normal University, Shanghai, China, [2]Department of Civil, Environmental, and Architectural Engineering, University of Padova, Padova, Italy, [3]Guangxi Key Laboratory of Marine Environmental Change and Disaster in Beibu Gulf, Beibu Gulf University, Qinzhou, China

Key Points:

- Shrub mangroves (SMs), with their lower canopy height, influence hydro-sedimentary processes differently from tree mangroves
- The full canopy submergence of SMs promotes favorable conditions for sediment accumulation at the front edge of the dense vegetation zone
- Vertical accretion at the fringe area facilitates conditions for mangrove seedling colonization and seaward vegetation expansion, supporting tidal flat stability

Supporting Information:

Supporting Information may be found in the online version of this article.

Correspondence to:

Z. Dai,
zjdai@sklec.ecnu.edu.cn

Citation:

Zhou, X., Dai, Z., Tognin, D., Luo, J., Wang, R., Feng, B., & Carniello, L. (2025). Shrub mangroves facilitate self-sustaining conditions for colonization: Insights from the Nanliu Delta, China. *Journal of Geophysical Research: Biogeosciences*, *130*, e2025JG008765. https://doi.org/10.1029/2025JG008765

Received 14 JAN 2025
Accepted 23 SEP 2025

Author Contributions:

Conceptualization: Xiaoyan Zhou, Zhijun Dai, Luca Carniello
Data curation: Xiaoyan Zhou, Luca Carniello
Formal analysis: Xiaoyan Zhou, Zhijun Dai, Davide Tognin
Funding acquisition: Zhijun Dai, Riming Wang, Luca Carniello
Investigation: Xiaoyan Zhou, Jiejun Luo, Riming Wang, Bingbin Feng
Methodology: Xiaoyan Zhou, Davide Tognin, Luca Carniello
Resources: Zhijun Dai
Visualization: Xiaoyan Zhou, Davide Tognin
Writing – original draft: Xiaoyan Zhou, Zhijun Dai
Writing – review & editing: Xiaoyan Zhou, Davide Tognin, Luca Carniello

© 2025. American Geophysical Union. All Rights Reserved.

Abstract Shrub mangrove (SM) tidal flats are vital ecosystems in tropical and subtropical regions, yet they are threatened by rising sea levels and anthropogenic activities. With their lower canopy height, SMs influence hydro-sedimentary processes differently from the well-studied tree mangroves, highlighting the need for a deeper understanding of the stability of the tidal flats they colonize. Here, we analyze hydrodynamic and sediment transport processes over a full spring-neap tidal cycle on an *Aegiceras corniculatum* tidal flat in the Nanliu delta China, to explore the bio-morphodynamic feedback shaping SM tidal flats. Our findings reveal distinct differences in hydrodynamics and sediment transport between the flood and ebb phases, with the flood phase playing a significantly stronger influence. During the flood phase, the interaction between tidal flow and increasing vegetation density landward results in a significant reduction in flow velocity (up to 36%), particularly concentrated at the vegetation fringe. This reduction diminishes sediment transport capacity (up to 80%), leading to a decline in suspended sediment concentration as it moves landward, resulting in localized deposition in front of the densely vegetated area. This process is further supported by the substantial vertical accretion observed over an annual timescale. Our observations reveal that sediment deposition at the front edge of the dense SM zone is associated with a coarsening of surface sediments, which creates favorable conditions for seedling establishment and drives seaward vegetation expansion. These findings highlight the critical role of SMs in coastal ecosystem resilience and the evolution of tidal flats.

Plain Language Summary Shrub mangroves are crucial ecosystems that colonize tropical and subtropical tidal flats. Unlike tree mangroves, shrub mangroves (SMs) interact with water flow and sediments throughout their entire structure, as they are fully submerged during high tides. However, the hydro-sedimentary processes within these ecosystems remain poorly understood. Here, we examine how SMs influence water flow and sediment transport on a tidal flat in the Nanliu delta, China. During flood tides—the most influential tidal phase—denser vegetation and larger plants interact with the water flow, promoting sediment deposition at the front edge of the dense SM zone. This sediment deposition leads to the accretion observed at the yearly timescale together with a shift toward rougher sediments characterized by a coarser grain size, which create favorable conditions for mangrove seedling establishment and seaward vegetation expansion. These findings deepen our understanding of how SMs shape their environments and enhance the resilience of coastal tidal flats.

1. Introduction

Mangroves typically inhabit estuaries, deltas, lagoons, and low-island regions in tropical to subtropical zones, where they contribute to tidal flat stabilization and shore protection by dissipating energy along shorelines (Ellison, 2019; Nguyen & Parnell, 2017; Temmerman et al., 2023; Tognin et al., 2019; Woodroffe et al., 2016). However, rising sea levels and increasing anthropogenic disturbances have made mangrove tidal flats one among the most vulnerable ecosystems (Jennerjahn et al., 2017; Ward et al., 2016). Given their multifunctional roles and the significant losses experienced in recent decades, understanding the interactions between mangrove vegetation and tidal flats is crucial for advancing knowledge on mangrove tidal flat evolution.

Mangroves exhibit a wide range of structural forms influenced by geophysical, geomorphological, and biological characteristics (Woodroffe, 1992). Mangrove heights vary significantly, often depending on salinity and nutrient availability (Lugo, 1989). Observed forms range from shrub-like growth to towering tree structures (Feller, 1995). Tree mangroves, typically found in equatorial regions with low cyclone activity and high precipitation, can reach heights of approximately 6–20 m (Simard et al., 2019). In contrast, shrub mangroves (SMs) generally remain

shorter than 1.5 m, with their physiology likely influenced by factors such as drought stress, salinity, nutrient limitation, tidal regime, and hydrological isolation (Cintrón et al., 1978; Cintrón & Schaeffer Novelli, 1984; Feller et al., 2003). Due to these environmental constraints, species with aerial roots may still exhibit characteristics typically associated with SMs (Anton et al., 2020; Lovelock et al., 2006; Reef et al., 2010). Swales et al. (2015) suggested that tree mangroves are more likely to establish on tidal flats with higher bed elevations, whereas SMs are found in slightly lower-elevation areas. Across the tidal flat, interactions between vegetation, tide flow, and sediment dynamics vary depending on local conditions.

The distinct physical structures of tree and SMs differently influence hydrodynamic processes on the tidal flats they colonize. Tree mangroves have been found to reduce tidal speed and amplitude by providing substantial drag with their aboveground root structures, stems, and the lower parts of canopies (Horstman et al., 2015; Montgomery et al., 2019). The substantial root systems of various mangrove species, such as the prop roots of *Rhizophora* spp., the plank roots of *Xylocarpus* spp. and *Heritiera* spp. (Krauss et al., 2014), and the pneumatophores of *Avicennia* spp. and *Sonneratia* spp., are recognized as some of the most influential structures in shaping hydro-sedimentary processes on tidal flats (Bird, 1986; Krauss et al., 2003). For instance, matrix root systems have been shown to enhance turbulent mixing, reduce peak velocity, and attenuate waves (Friess et al., 2012; Norris et al., 2019; Tomiczek et al., 2020; Yoshikai et al., 2022). In contrast, SMs, with their lower stature and a higher canopy cover, are characterized by a wider-angled canopy and a longer hydroperiod (Kauffman & Donato, 2012; Lugo & Snedaker, 1974) than tall species. Turbulence within vegetation canopies can play an important role in suspending sediment (Tinoco & Coco, 2016). Therefore the contrast in aboveground vegetation traits of shrub and tree mangroves must be accounted for, given their distinct influences on hydrodynamic processes.

The interaction between water flow and vegetation structures significantly influences sedimentation patterns (Carniello et al., 2016; Ellison, 2009). To assess the vegetation influence on tidal flat morphology, it is crucial to understand how hydrodynamic and sediment transport processes respond to varying vegetation configurations, with particular emphasis on SMs. However, the effects of SMs cannot be directly inferred from existing bio-geomorphological knowledge derived from tree species, as their interactions with flow and sediment dynamics are notably different. Thus, an in-depth study into the hydro-sedimentary process of a tidal flat colonized by SMs may reveal previously neglected insights.

Among the different SM species, *Aegiceras corniculatum* (*AC*), which colonizes the coastal regions of Southwest China, provides a representative setting to observe hydrodynamic-sedimentary processes within partly or fully submerged vegetation of SMs. As a pioneer species with stress-resistant traits, *AC* can survive under harsh conditions (Adame et al., 2021; Peng et al., 2015), yet it is also among the first species likely to be impacted by rising sea levels. This makes the geomorphology of *AC*-colonized tidal flats particularly noteworthy among shrub-like mangrove ecosystems. In our study, SMs specifically refer to individuals lacking aerial roots.

This work aims to (a) characterize the spatiotemporal patterns of hydrodynamics and sediment dynamics within an SM tidal flat in Southwest China, anticipating that these processes are closely linked to SMs distribution, (b) investigate the influence of SM structures and densities on sedimentation patterns, hypothesizing that denser and more complex SM structures enhance sediment stabilization, and (c) elucidate the role of SMs in shaping the morphological evolution of tidal flats, revealing if SM stabilization promotes accretion and contributes to long-term resilience. Our findings highlight how SMs can contribute to the stabilization and protection of intertidal zones against flooding, potentially creating more favorable conditions for mangrove colonization and expansion. This enhanced understanding of mangrove-vegetated tidal flat dynamics may offer valuable insights to guide effective restoration and management strategies.

2. Data Acquisition

2.1. Study Site

The Nanliu delta is located in the northwestern region of the South China Sea, and it is the largest delta in the southwest of China (Figure 1a). The delta is subject to irregular diurnal tides, with an average tidal range of 2.46 m and a maximum of 5.36 m (Committee of Annals of Chinese Estuaries, 1998), and it has an average annual water discharge of 166 $m^3 \cdot s^{-1}$ and sediment discharge of 2.81×10^{-3} $kg \cdot s^{-1}$ (Zhou et al., 2022). In this setting, we established five measurement stations along a transect, aligned as closely as possible with the flood tide direction (Figure 1c). We selected flood tide direction as a representative, because of the much larger velocities than the ebb

21698961, 2025, 10, Downloaded from https://agupubs.onlinelibrary.wiley.com/doi/10.1029/2025JG008765 by Zhijun Dai - East China Normal University , Wiley Online Library on [24/10/2025]. See the Terms and Conditions (https://onlinelibrary.wiley.com/terms-and-conditions) on Wiley Online Library for rules of use; OA articles are governed by the applicable Creative Commons License

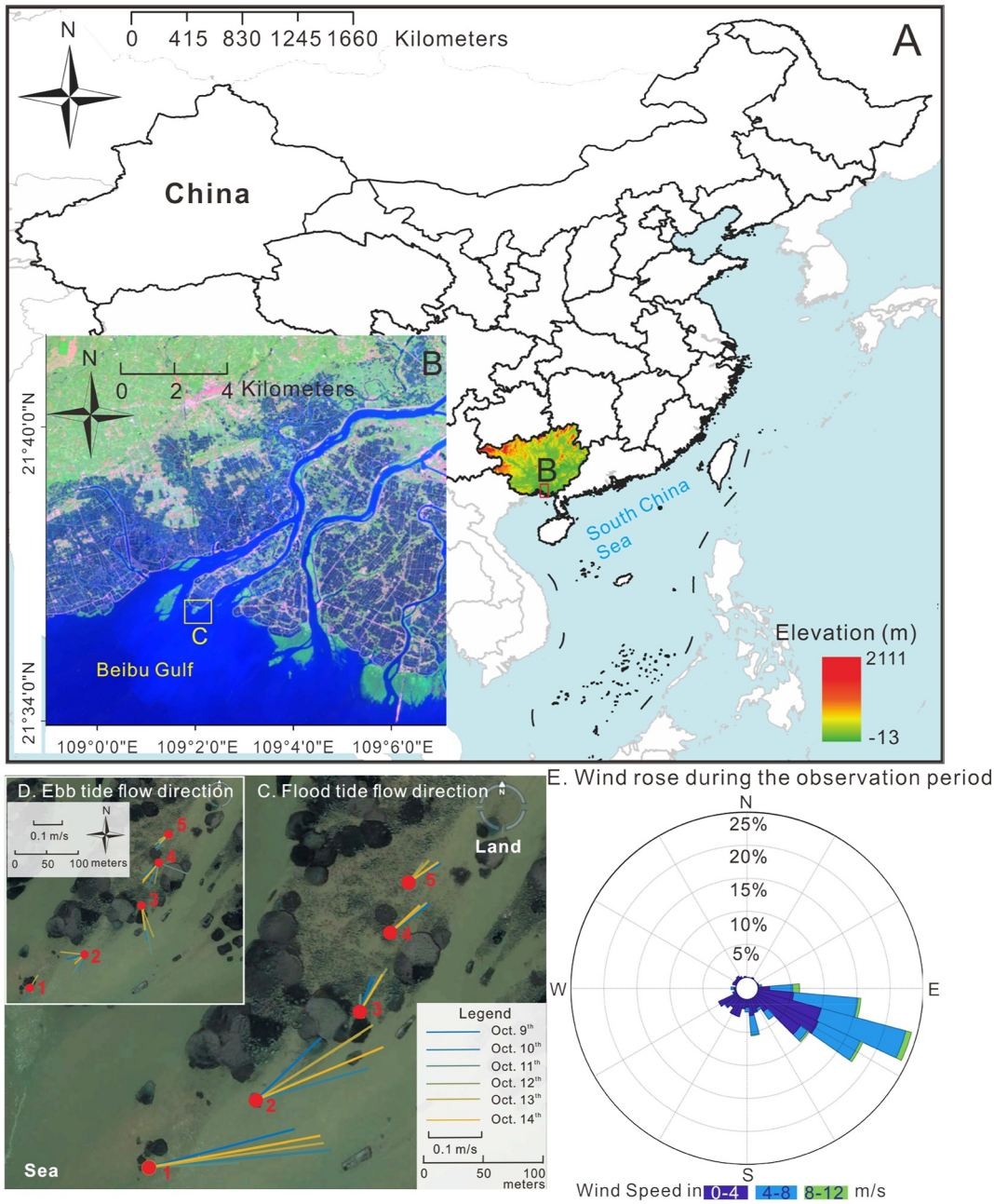

Figure 1. (a) Map of the Nanliu delta with its location in relation to China and the South China Sea. (b) Study area. (c) Flow directions during six flood tidal cycles across five observation stations. (d) Flow directions during six ebb tidal cycles across five observation stations. (e) Wind rose distribution during the observation period (Pereira, 2025).

tide (Figures 1c and 1d). Along this transect, SMs of varying ages and density distributions are present. The selection of the transect also considered the accessibility for instrument maintenance and data retrieval at each station.

Wind data for the area were acquired from the European Centre for Medium-Range Weather Forecasts (ECMWF). Throughout the monitoring period from 9 to 14 October 2021, the wind predominantly blew perpendicular to the transect, from the east (E) and east southeast (ESE), with lower wind speeds of 3.9 $m \cdot s^{-1}$ (Figure 1e) on average. These mild meteorological conditions, characterized by an annual mean wind velocity of 2.67 $m \cdot s^{-1}$ (See Figure S1 in Supporting Information S1), result in negligible wave activity, with an annual mean

21698961, 2025, 10, Downloaded from https://agupubs.onlinelibrary.wiley.com/doi/10.1029/2025JG008765 by Zhijun Dai - East China Normal University , Wiley Online Library on [24/10/2025]. See the Terms and Conditions (https://onlinelibrary.wiley.com/terms-and-conditions) on Wiley Online Library for rules of use; OA articles are governed by the applicable Creative Commons License

Table 1
Vegetation Parameters

Station No.	Size classification	N	H_v (m)	r (m)
1	S	11	0.69	0.2
2	S	6	0.61	0.17
3	M	8	0.62	0.23
	L	10	0.93	0.5
4	M	20	0.7	0.23
	L	7	0.94	0.54
5	M	14	0.6	0.25
	L	3	0.82	0.55

wave height of approximately 0.3 m (Zhou et al., 2022). Such conditions provide a favorable environment for mangrove colonization and expansion along the tidal flat, offering an ideal opportunity to observe their interaction with hydro-sedimentary processes.

2.2. Data and Methods

Vegetation along the study transect is composed of SM *AC* individuals of varying sizes. Station 1, located at the offshore end of the study transect, was positioned on the unvegetated tidal flat. The other four observation stations were installed at distances of 110, 240, 330, and 390 m landward from Station 1, following a gradient of increasing SM density and size (Figure 1c). Along the 390 m transect, elevation ranged from 0.20–0.43 m relative to the local mean sea level, with a mean slope of 0.058%. Two quadrats of 5 × 5 m^2 located close to each observation station were selected to measure vegetation density and characteristics. SMs within each quadrat were randomly selected and measured using a measuring tape to characterize the plant features within the plot. The height (H_v) and the canopy radius (r) of each plant were measured (Table 1), and the average values were used to represent the vegetation dimensions at each observation station. Additionally, the number of plants (N) in each quadrat was counted to calculate the vegetation density. Based on these measurements, a histogram was plotted to show the distribution of canopy projected area on the ground (S_v) in relation to the corresponding number of plants (Figure 2a). Figure 2a presents the size classification of all *AC* along the transect, based on canopy area and the plant count. The three probability peaks observed in the histogram allowed us to categorize all plants along the transect into three categories according to their canopy areas. Vegetation at Stations 1 and 2 is characterized by the presence of only small plants, whereas Stations 3, 4, and 5 contained both medium- and large-sized plants (Table 1). After determining the representative vegetation dimensions for each size class (small, medium, and large), we schematized each *AC* plant as an upside-down cone to represent each size category (Figure 2b). Vegetation at each station was then characterized by the observed vegetation density (number of upside-down cones per unit area) and plant class.

The submerged solid volume fraction (*SVF*) at each station is used as an index to represent the portion of the water column occupied by vegetation, based on the local water depth (Maza et al., 2019; Xu et al., 2022; Zhou et al., 2022). *SVF* is calculated as

$$\mathrm{SVF} = \text{Submerged forest volume}/\text{Water volume} \tag{1}$$

To calculate the submerged forsest volume, three key parameters are required: the radius of a single plant canopy (r), the height of a single plant (H_v), and the number of plants (N) within the quadrat. The *SVF* at the 5 stations, as

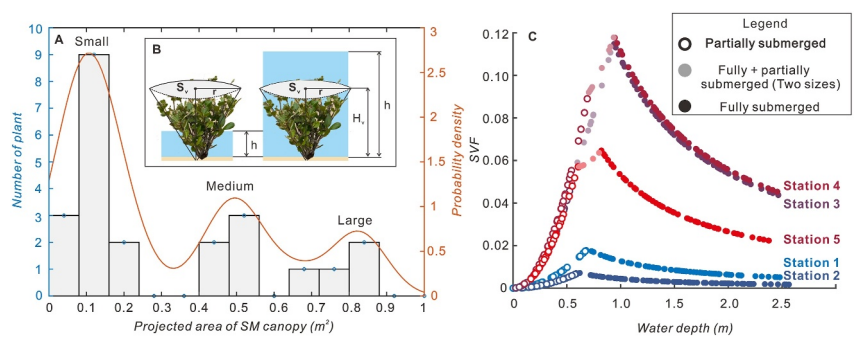

Figure 2. (a) Histogram of canopy areas from the typical *AC*s, which were measured along the study transect. Based on the three peaks from the distribution, small, medium, and large sizes of the *Aegiceras corniculatum (AC)* can be classified. (b) Generalization of the method to get vegetation parameters from the field. (c) Submerged volume fraction of the *AC* changed with water depth fluctuation. Empty dots refer to the scenario of *AC*s being partially submerged. The semitransparent dots represent the scenario at Stations 3, 4, and 5, where there are two sizes of vegetation: the smaller vegetation is completely submerged, while the larger vegetation is only partially submerged. The solid points represent the scenario where all vegetation is completely submerged. The sketch bases on the real scenario in the field.

21698961, 2025, 10, Downloaded from https://agupubs.onlinelibrary.wiley.com/doi/10.1029/2025JG008765 by Zhijun Dai - East China Normal University , Wiley Online Library on [24/10/2025]. See the Terms and Conditions (https://onlinelibrary.wiley.com/terms-and-conditions) on Wiley Online Library for rules of use; OA articles are governed by the applicable Creative Commons License

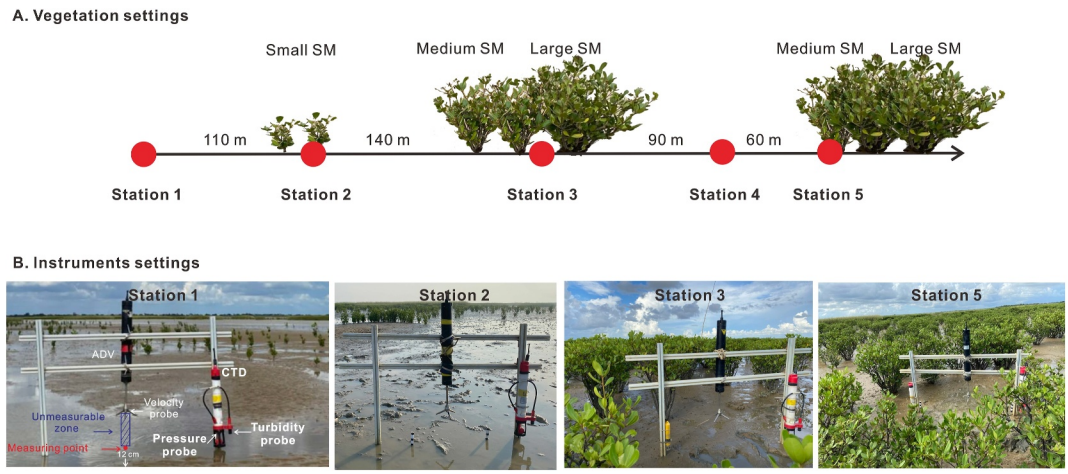

Figure 3. (a) Vegetation settings along the transect. (b) Instrument settings at Stations 1, 2, 3, and 5.

a function of the local water depth, is presented in Figure 2c and will be discussed in the following section. For further details on the calculation, refer to the Supporting Information S1.

Flow velocity, turbidity, and water depth were also measured at the five stations from 9 to 14 October 2021, covering a spring-neap tidal cycle along the transect (Figure 3a). Instruments were mounted on stainless steel frames, which were inserted approximately 1.5 m into the bed at each station. All sensors were submerged during the tidal cycle, and all the setting details are listed in Table 2.

An acoustic Doppler velocimeter (ADVs, 6.0-MHz, Nortek Vector, Norway) was deployed at each station down-looking, to measure high-resolution (16 Hz) velocities in east-west (u), north-south (v), and up-down (w) directions, at 0.12 m above the bed (considered as near-bed velocities). The ADV transmitters were all installed at 0.27 m above the bed, allowing for a blanking distance of 0.15 m (Figure 3b). Raw flow velocities recorded by ADV at 16 Hz were postprocessed through filtering, phase-space thresholding method, and burst averaging. Specifically, a 70% correlation threshold was set up to filter the raw data (Rusello et al., 2006). Spikes at the high sampling record were then interpolated via the phase-space thresholding method (Goring & Nikora, 2002). Following the Reynolds decomposition, the instantaneous flow velocity components (u, v, and w) were decomposed into time-averaged ($\overline{u}$, $\overline{v}$, and $\overline{w}$) and fluctuating (u', v', and w') quantities. The turbulent kinetic energy (TKE) is then calculated as TKE $= \left(u'^2 + v'^2 + w'^2\right)/2$. Subsequently, the smoothed velocities were burst-averaged (measuring 512 s $\times$ 16 = 8,192 samples in 30 min) to get the mean velocity within a burst. Based on prior field studies within mangroves (Horstman et al., 2015), the profile-averaged speed (U) is computed as $U = 1.3 \times \sqrt{u^2 + v^2 + w^2}$.

A conductivity-temperature-depth—CTD—sensor (RBRconcerto^3, Canada) equipped with an additional turbidity sensor, was used to monitor water depth (precision ±10 mm) and turbidity along the transect. Data were collected continuously at 1 Hz, with average values computed every 2 min (120 samples).

Turbidity measurements, originally measured in nephelometric turbidity units, were subsequently converted to suspended sediment concentration (SSC) through calibration conducted in the laboratory using bed material collected near each observation station. Good correlations (R^2 = 0.98–0.99) between SSC and turbidity were found for each sensor, modeled using a second-order polynomial function (Figure S2 in Supporting Information S1).

Table 2
Instruments Settings

	Data	Measuring mode	Sampling frequency (Hz)	Samples per burst, burst interval (min)
ADV	Flow velocity (*u, v, and w*)	Burst	16	8,192, 30
CTD	Turbidity and water depth	Continuous	1	1, 2

21698961, 2025, 10, Downloaded from https://agupubs.onlinelibrary.wiley.com/doi/10.1029/2025JG008765 by Zhijun Dai - East China Normal University , Wiley Online Library on [24/10/2025]. See the Terms and Conditions (https://onlinelibrary.wiley.com/terms-and-conditions) on Wiley Online Library for rules of use; OA articles are governed by the applicable Creative Commons License

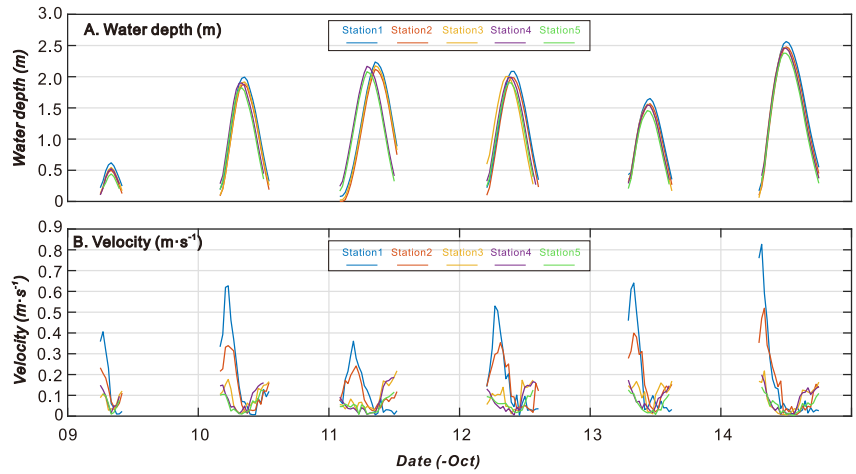

Figure 4. (a) Water depth and (b) velocity data from Stations 1 to 5, respectively.

The total suspended sediment fluxes per unit area (q_s) at each station were then computed as

$$q_s = \mathrm{SSC} \times U \tag{2}$$

where SSC is the mean concentration of suspended sediment (kg·L^{-1}) and U is the mean velocity (m·s^{-1}) at the corresponding time (Glover et al., 2022).

To analyze sedimentation characteristics along the transect, two batches of surface sediments (1.5–2 cm depth) were collected at 10-m intervals moving landward, starting from Station 1. The first round of bed sampling was conducted in January 2021, focusing on the initial portion of the transect from Station 1 to Station 3, where the boundary between the bare and the vegetated tidal flat was located. In November 2021, bed sediment sampling was repeated and extended 110 m landward of Station 3, reaching up to Station 5, to capture areas with denser and larger plant vegetation. The grain size of the surface sediment was analyzed via a laser diffraction analyzer (Malvern Mastersizer 3000). The sediment sorting result is determined according to the Folk and Ward (1957) method. A manual RTK-GPS was also used to measure bed elevation along the transect at each sampling location. The measured bed elevations were referenced to the average mean sea level of Beihai ($\mathrm{MSL_{BH}}$), which was used as a reference datum.

3. Results

3.1. Inundation States of the Shrub Mangroves

Unlike tree mangrove species for which only the trunk and the aboveground root systems are usually flooded, all the SMs along our monitoring transect experienced partially/fully submerged state according to the local water level (Figure 2c). Six tidal cycles were recorded from 9 to 14 October 2021, with mean water depth values of 0.36, 1.14, 1.21, 1.23, 1, and 1.51 m, respectively. The water depth did not vary significantly among the 5 stations during the single tidal cycle and, apart from the first day of monitoring (9th October), the maximum water depth was maintained relatively constant during the remaining days of survey (Figure 4a). The average water depths over the entire observation period for Stations 1 to 5 were 1.03, 1.13, 1.07, 1.10, and 1.04 m, respectively, and the instantaneous values varied almost simultaneously at all the stations within each tidal cycle.

The computed *SVF* at the 5 stations varies as a function of the local water depth (Figure 2c). For the first two seaward stations, *SVF* increases as water depth increases up to 0.6 m (i.e., the height of the canopy for the small size class of SM). During this phase, the volume of submerged structures increases, leading to a greater influence of the vegetation on water flow. However, once the water depth exceeds the canopy height, the influence of vegetation on the water column gradually diminishes with a further increase in water depth. At Stations 3, 4 and 5, which contain both medium and large vegetation, the variation in *SVF* follows three distinct stages. Initially, when the water depth is below the canopy height of both vegetation types (up to 0.62 m), *SVF* increases proportionally

21698961, 2025, 10, Downloaded from https://agupubs.onlinelibrary.wiley.com/doi/10.1029/2025JG008765 by Zhijun Dai - East China Normal University , Wiley Online Library on [24/10/2025]. See the Terms and Conditions (https://onlinelibrary.wiley.com/terms-and-conditions) on Wiley Online Library for rules of use; OA articles are governed by the applicable Creative Commons License

Table 3
Average v, Suspended Sediment Concentration, and q_s ($kg \cdot m^{-2} \cdot s^{-1}$) at Every Station During Flood and Ebb Tides

		Sta.1	Sta.2	Sta.3	Sta.4	Sta.5
v ($m \cdot s^{1}$)	Flood (F)	0.28	0.21	0.076	0.066	0.058
	Ebb (E)	0.04	0.07	0.11	0.101	0.06
	F/E	7.07	2.94	0.69	0.65	0.98
SSC ($kg \cdot L^{-1}$)	Flood (F)	1.64	2.11	0.41	0.31	0.15
	Ebb (E)	1.35	1.88	0.33	0.28	0.11
	F/E	1.22	1.12	1.25	1.09	1.40
q_s ($kg \cdot m^{-2} \cdot s^{-1}$)	Flood (F)	0.38	0.35	0.028	0.017	0.008
	Ebb (E)	0.04	0.11	0.026	0.019	0.004
	F/E	9.08	3.42	1.09	0.87	2

with water depth. When the medium-sized SM is fully submerged, but the large-sized SM remains partially emergent (water depth between 0.62 and 0.9 m), the rate of *SVF* increase slows down. Finally, when both medium and large SM are fully submerged (the water depth exceeding 0.9 m), *SVF* begins to decline. The variation in *SVF* as a function of the water depth, shown in Figure 2c, effectively demonstrates *SVF*'s capability to describe conditions with mixed plant geometries.

3.2. Flow Velocity

From seaward to landward, the average measured bed flow velocity (U) decreased progressively, with values of 0.17, 0.14, 0.09, 0.08, and 0.06 $m \cdot s^{-1}$, respectively, along the transect. The most significant velocity reduction occurred between Station 2 and 3, where it dropped by a factor of 1.6 (Table 3).

The emergence of denser and taller SM at Station 3 produced a notable change in the spatiotemporal dynamics of flow velocity between the two seaward stations and the three landward stations (Figure 4b). At the seaward stations, bed flow velocities showed a pronounced asymmetry between the flood and the ebb tidal phase with flood velocities significantly higher than ebb velocities (Table 3). In contrast, at the landward stations, U exhibited a more symmetric pattern, with little variation between flood and ebb phases. The flow asymmetry was quantified by the ratio of average flood flow speed to ebb flow speed with values approaching 1 indicating similar bottom flow intensity during both phases. As vegetation density increases landward along the transect, flood flow is increasingly mitigated by SM patch, while the ebb flow remains spatially consistent. This shift results in a transition from flood-dominant to ebb-dominant conditions, with the ratio of average flood to ebb flow speed decreasing from 7.07, 2.94, 0.69, 0.65, and finally 0.96 moving landward.

Additionally, the turbulent kinetic energy (TKE) at each station was computed to estimate turbulence induced by the bottom velocity, shown in Figure 5, alongside *SVF* values. During the flood phase of the tide, the average *TKE* value at Station 1 and 2 is approximately 2–3 times higher than at the landward stations, while the corresponding *SVF* values are about 4–5 times lower (Figure 5a). During the ebb tide, *SVF* values remain similar to those during the flood tide, but in this case, the flow is directed seaward. *TKE* values at Station 5, 4, and 3 remain lower than the flood phase, due to the presence of dense, large vegetation, which significantly limits the current's ability to resuspend sediment. Outside the vegetated area, the flow is unobstructed, but as shown by Figure 5b, *TKE* across all five stations becomes nearly uniform, with only a slight increase at Station 1. This increase may be partially attributed to the slight misalignment of the flow with the transect, particularly at the seaward portion near Station 1 during the ebb tide (see Figure 1d).

3.3. Sediment Transportation Features

Turbidity along the SM transect was measured simultaneously to flow velocity and converted into SSC after calibration (see Figure S2 in Supporting Information S1). Strong tidal currents (Figure 4) transported a significant

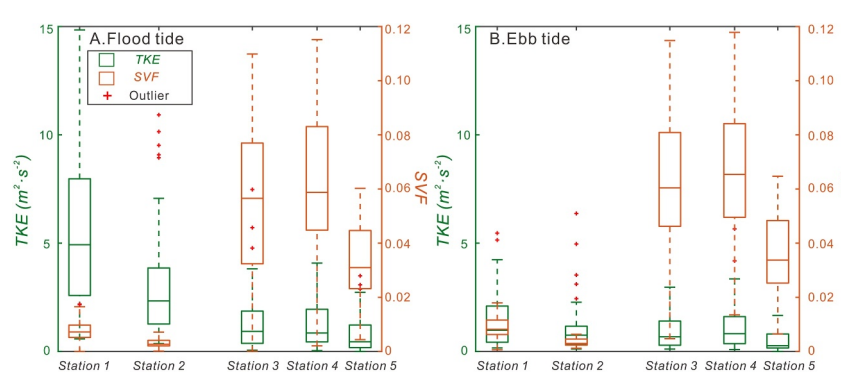

Figure 5. The bottom *turbulent kinetic energy* and SVF values at each station during the (a) flood tide and the (b) the ebb tide.

21698961, 2025, 10, Downloaded from https://agupubs.onlinelibrary.wiley.com/doi/10.1029/2025JG008765 by Zhijun Dai - East China Normal University , Wiley Online Library on [24/10/2025]. See the Terms and Conditions (https://onlinelibrary.wiley.com/terms-and-conditions) on Wiley Online Library for rules of use; OA articles are governed by the applicable Creative Commons License

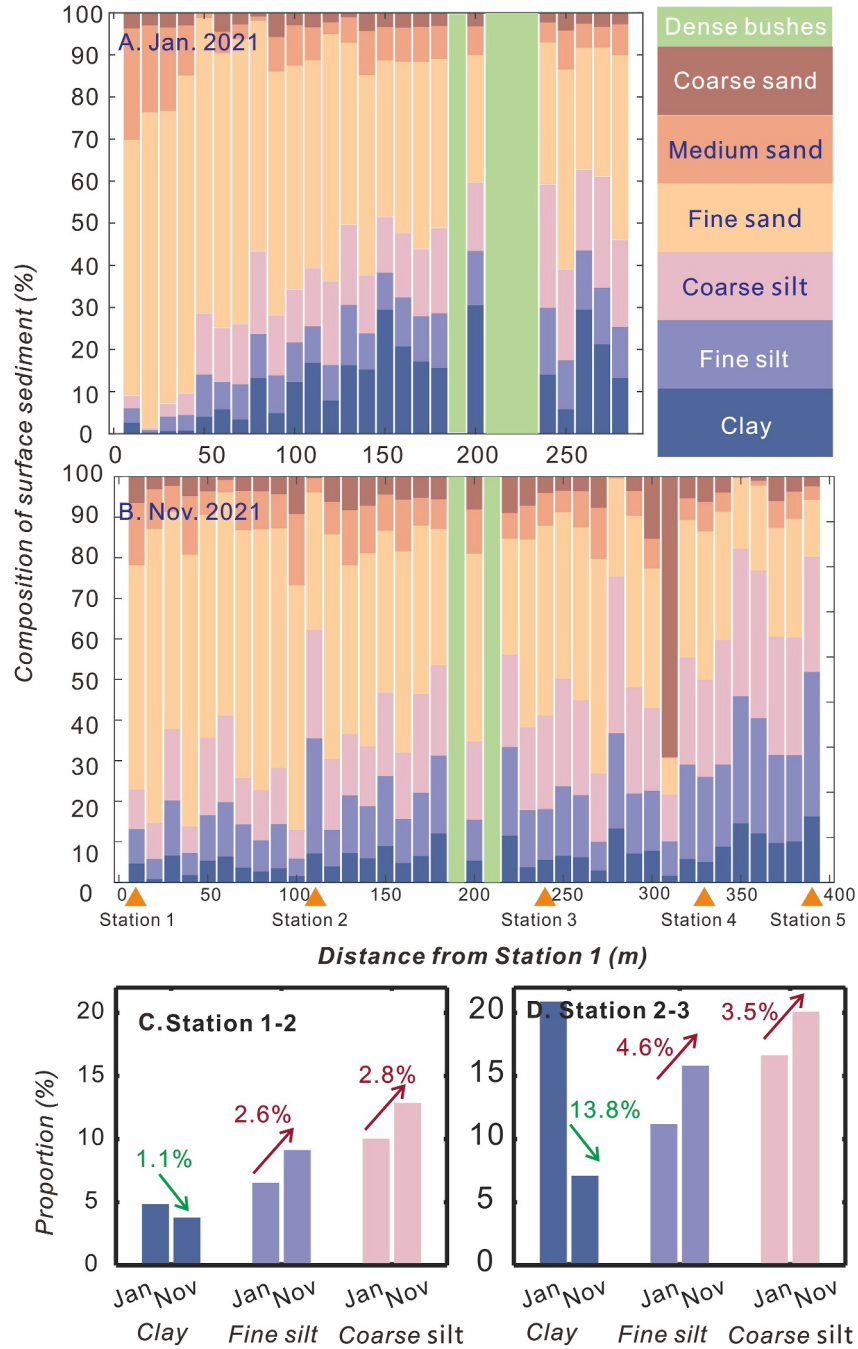

Figure 6. Surface sediments were collected every 10 m along the transect except dense bush regions at (a) January and (b) November 2021, respectively. (c) The variation pattern of clay, fine silt, and coarse silt components were exhibited with their value.

amount of sediment toward the SM tidal flat during flood tide (Table 3 and Figure 6a). Starting from the seaward end of the transect, SSC increased from 1.5 kg·m^{-3} at Station 1 to 2 kg·m^{-3} at Station 2. However, within the densely vegetated SM region, encompassing Stations 3, 4, and 5, SSC sharply decreased to 0.37, 0.29, and 0.13 kg·m^{-3}, respectively. The transition from the sparsely vegetated tidal flat to the dense SM patch, between Station 2 and 3, caused an approximately 80% reduction in SSC (Figure 6a). This drop in sediment concentration coincided with a reduction in flow velocity, suggesting that the lower velocities in this region were insufficient to maintain sediment suspension or mobilize local bed material.

21698961, 2025, 10, Downloaded from https://agupubs.onlinelibrary.wiley.com/doi/10.1029/2025JG008765 by Zhijun Dai - East China Normal University , Wiley Online Library on [24/10/2025]. See the Terms and Conditions (https://onlinelibrary.wiley.com/terms-and-conditions) on Wiley Online Library for rules of use; OA articles are governed by the applicable Creative Commons License

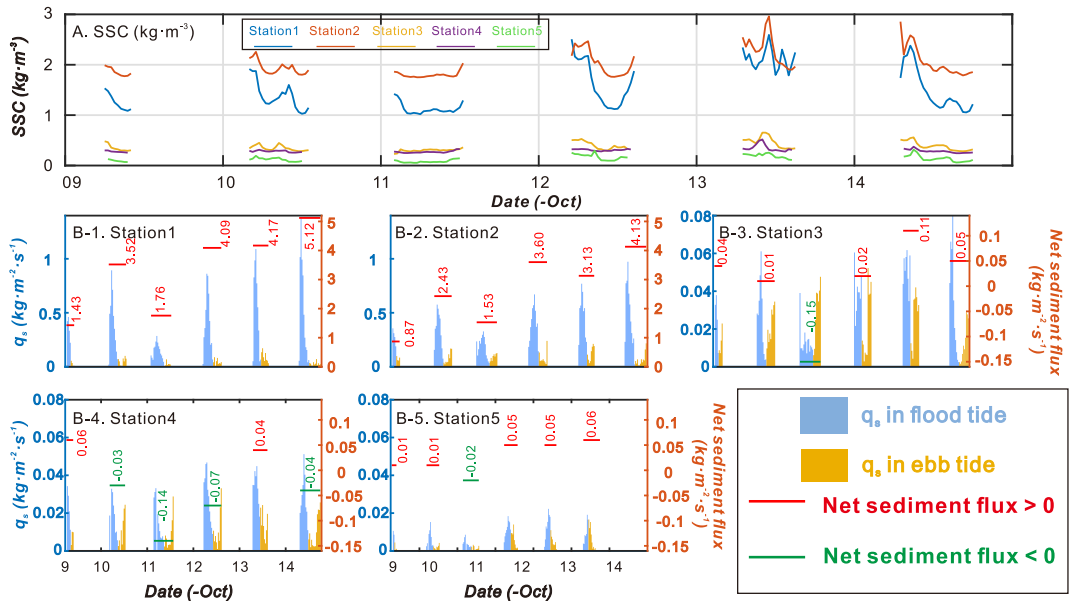

Figure 7. (a) Suspended sediment concentration and (b) suspended sediment flux (q_s) from Stations 1 to 5 during flood tide (a) and ebb tide (b) along the transect., respectively.

The analysis of sediment fluxes per unit area (q_s) revealed a distinct sediment pattern along the transect (Figure 6b). At Stations 1 and 2 (Figures 5b2 and 6b1), flood tides played a dominant role in transporting sediment from the seaward direction, with fluxes of 0.38 and 0.35 kg·m^2·s^{-1}, respectively, while ebb tide sediment fluxes were lower (0.04 and 0.11 kg·m^{-2}·s^{-1}, respectively). The region between Station 2 and 3 exhibited a buffering effect on sediment flux, similar to the effect observed for flow velocity (U) and SSC. At Station 3, 4, and 5, q_s dropped sharply to 0.028, 0.017, and 0.008 kg·m^{-2}·s^{-1} respectively, which were 10 times lower than at Station 1 and 2 (Figures 6b3, 6b4 and 6B5). Ebb tides were too weak to mobilize bed sediments. The variation in q_s between stations during flood and ebb tides resulted in distinctive sedimentation characteristics along the transect, particularly at the edge part of SM patch.

3.4. Sedimentation Dynamics in the SM Fringe Area

The properties of surface sediments along the transect were analyzed in January 2021 and in November 2021, and they were categorized into clay, silt, and sand, exhibiting distinct spatial and temporal variations (Figures 7a and 7b). By observing grain size spatially, the sedimentation results show a finer trend moving landward. Starting from Station 1 to 3, fine sand and medium sand dominated the sparsely vegetated areas and vegetation fringe, while finer sediments, such as clay and silt were more prevalent at Station 4 and 5.

Notably, there was an overall increase in the proportion of coarser sediments between Station 2 and 3 over one year. At the edge of the vegetated area, clay content decreases by 13.8% while fine and coarse silt increase by 4.6% and 3.5%, respectively (Figure 7d). This shift indicates an ongoing coarsening of bed composition happening within the vegetated region over time. The comparison suggests that SM density influences sediment textural patterns, promoting the accumulation of coarser sediments (fine and coarse silt) close to the fringe mangrove patch, while finer sediments (clay) dominate at Stations 4 and 5.

4. Discussion

4.1. Hydrodynamic Effect on Sediment Transportation Over the SM

Our results show a clear link between SM canopy parameters and hydro-sedimentary variables from our monitoring transect where the mangroves experience full submersion during high tide, leading to complete interaction with water flow and sediment (Figure 2c) and confirming that SMs affect the hydrodynamic and sedimentation processes. As discussed in Section 3.3, SSC decreases rapidly moving landward along the transect (Figure 6a) particularly at the edge of the densely vegetated area, indicating a strong influence of the vegetation on

21698961, 2025, 10, Downloaded from https://agupubs.onlinelibrary.wiley.com/doi/10.1029/2025JG008765 by Zhijun Dai - East China Normal University , Wiley Online Library on [24/10/2025]. See the Terms and Conditions (https://onlinelibrary.wiley.com/terms-and-conditions) on Wiley Online Library for rules of use; OA articles are governed by the applicable Creative Commons License

both hydrodynamics and sediment dynamics. Specifically, the lower and rapidly submerged SM canopy actively retains sediment at the fringe of the vegetation patch during the flood phase. In contrast, in areas colonized by tree mangroves, the water level rarely reaches the canopy, but water flow typically interacts with their aboveground root systems, which are characteristic of these species. Aerial roots exhibit various shapes and sizes, with the "pencil" form predominantly associated with *Sonneratia* and *Avicennia* species. These roots can enhance microscale turbulence, influencing the vertical distribution of sediment within the water column. The eddies and vortices generated by these roots accelerate flow and resuspend bed sediment at the edges of vegetation patches. Meanwhile, the landward portion of the vegetation patch is sheltered by denser and larger roots or plants, facilitating the transport of finer sediments from outside the mangrove forest into its interior (Mullarney et al., 2017). This phenomenon is also observed in flume experiments. According to Cheng et al. (2020) and Xu et al. (2022), turbulence generated by obstacles like pipes or cylindrical vegetation, similar in effect to the trunk and prop roots of tree mangroves, can enhance sediment entrainment. These contrasting behaviors underscore the crucial role of vegetation physiology in sediment transport processes, highlighting that insights drawn from much taller mangrove species cannot be directly applied to SMs without careful consideration.

Our findings indicate that most suspended sediment transported by flood tides is deposited between Station 2 and 3 (Figure 6c), where there is a sudden increase in mangrove size and density. As shown in Figure 5, the combination of high *TKE* and low *SVF* demonstrates the ability of flood currents to entrain and transport sediment in suspension from the seaward tidal flat toward the SM patch. However, at the edge of the densely vegetated area, where *SVF* increases, bottom *TKE* decreases, reducing the sediment transport capacity. This, combined with the ability of the submerged mangrove canopy to trap a large portion of suspended sediment, promotes sediment deposition at the mangrove margin. During the ebb tide, the inherently lower *TKE* further limits sediment resuspension, allowing the sediment deposited at the seaward edge of the SM patch during the flood phase to remain in place.

4.2. Sediment Pattern Over the SM Tidal Flat

Based on the spatiotemporal variations in *TKE* and *SVF* during flood and ebb tides across different stations (Figure 5), the net sediment transport process at the edge of the dense SM patch, particularly between Stations 2 and 3, reveals a reduction in sediment transport between flood and ebb tides (Figure 8). The decreased *TKE* and increased *SVF* explain the reduction in sediment flux during the flood phase of the tide from the seaward region to the edge of the densely vegetated area (Figure 8a). Interestingly, despite the relatively constant *TKE* pattern along the transect during ebb phases, the sediment flux per unit area shows a notable reduction seaward of the SM patch, between Stations 3 and 2, even though the magnitude of this process is about an order of magnitude lower during the ebb compared to the flood phase (Figure 8b). This localized decrease in sediment transport capacity at the edge of the SM patch is associated with increased deposition of coarser sediment. Observing the elevation changes along the transect between January and November 2021 reveals significant accretion at the front edge of the SM patch, with an increase of 4.17 cm between Stations 1 and 2 and 2.47 cm between Stations 2 and 3 (Figure 8c). These findings align with sedimentation patterns inferred from field data, indicating that deposition primarily occurs during the flood phase when sediment transport capacity at the seaward edge of the vegetated area undergoes significant reduction. This confirms that denser and more complex SM structures enhance sediment deposition. During the ebb phase, flow directions (Figure 1d) suggest that sediments transported from Station 3 to Station 2 may deviate from their original along-transect path due to the abrupt decrease in vegetation density. As a result, under the monitored conditions, some sediments transported across the vegetated portion of the transect (Stations 5, 4, and 3) during the ebb phase may not reach Stations 2 and 1. Additionally, flow directions in Stations 1 and 2 (Figure 1d) suggest the possibility of an external sediment contribution not directly linked to along-transect sediment transport during the ebb phase but delivered by the adjacent tidal channel. This external input may account for the greater accretion observed at Station 1 compared to Station 2.

In the context of sedimentary features over a spring-neap tidal cycle, the sediments at the patch edge have become coarser (Figures 7b and 7c). More energetic offshore tidal currents (Figure 4b) transport sediments into the inshore region where the transect is located. As tidal energy dissipates during propagation, coarser sediments tend to settle due to the reduced sediment-carrying capacity. Based on our measurements, this capacity declines sharply near the densely vegetated area, allowing only finer sediments to move further landward and reach the end of the transect. A coarser bed composition enhances soil porosity, aeration, and infiltration capacity, creating a more favorable environment for the growth of mangrove seedlings (Gill & Tomlinson, 1977; Kozlowski, 1999;

21698961, 2025, 10, Downloaded from https://agupubs.onlinelibrary.wiley.com/doi/10.1029/2025JG008765 by Zhijun Dai - East China Normal University , Wiley Online Library on [24/10/2025]. See the Terms and Conditions (https://onlinelibrary.wiley.com/terms-and-conditions) on Wiley Online Library for rules of use; OA articles are governed by the applicable Creative Commons License

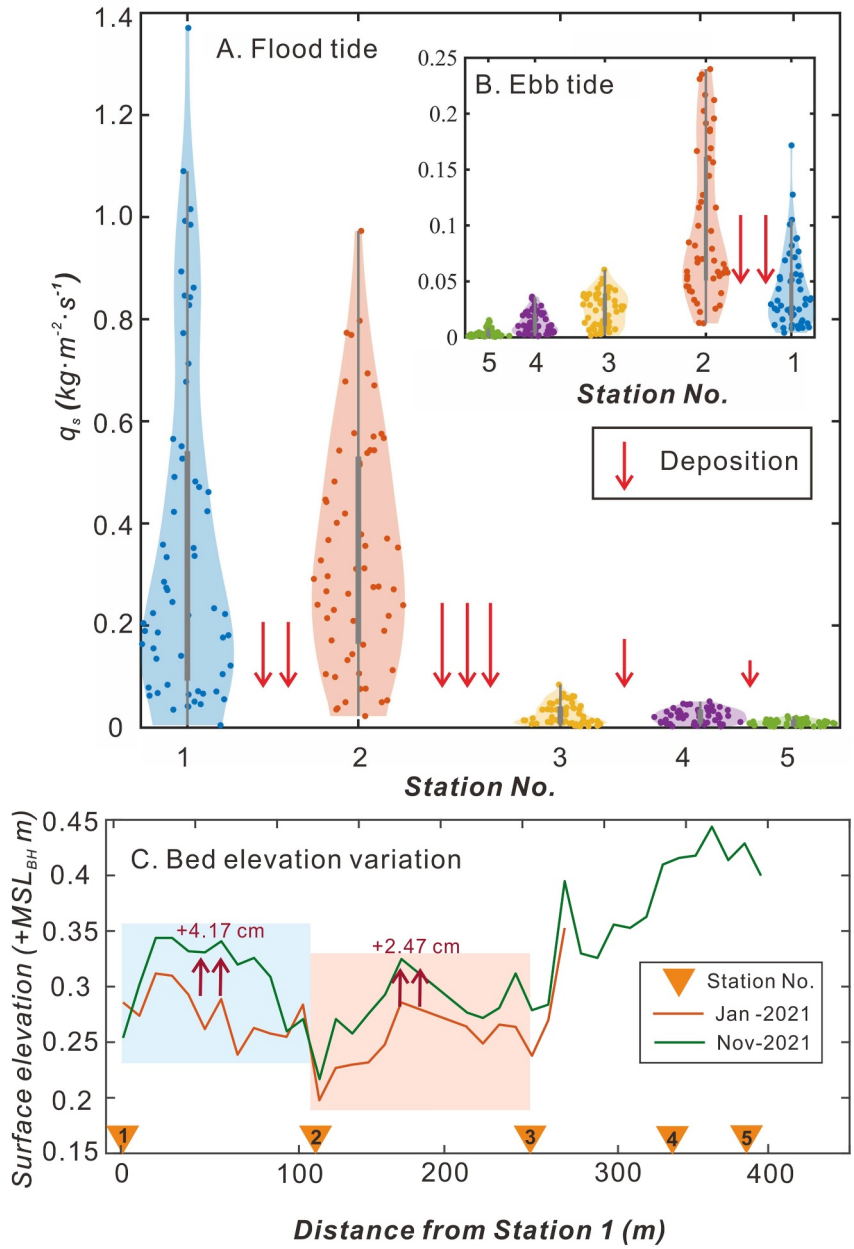

Figure 8. (a) and (b) are the sketches of sediment deposition processes at different areas based on the q_s (Bechtold, 2025). (c) Mean surface elevation at the edging part of the tidal flat from January to November 2021. Accretion between Stations 1 and 2 was higher than the value between Stations 2 and 3, which was 4.17 and 2.47 cm, respectively.

Krauss et al., 2003). As seedlings at the edge grow, the size and density of the SM increase, promoting the seaward expansion of the vegetation patch. This suggests the establishment of a positive feedback loop, given a sufficient sediment supply, in which localized deposition fosters vegetation expansion, which in turn promotes further sediment deposition moving seaward. Long et al. (2022) identified mangrove expansion in the Nanliu delta from 1998 to 2020 using remote sensing imagery. This seaward advancement of the SM patch is further supported by a comparative analysis of satellite images from 2014, 2019, and 2021 (See Figure S3 in Supporting Information S1). However, mangroves are insufficient in stabilizing or promoting coastal resilience in areas with limited sediment supply or under highly energetic hydrodynamic conditions (Besset et al., 2019). Conversely, mangroves with an extensive aboveground root system may increase local turbulence, enhance bed erosion, and accelerate shoreline retreat (Gajre et al., 2024).

21698961, 2025, 10, Downloaded from https://agupubs.onlinelibrary.wiley.com/doi/10.1029/2025JG008765 by Zhijun Dai - East China Normal University , Wiley Online Library on [24/10/2025]. See the Terms and Conditions (https://onlinelibrary.wiley.com/terms-and-conditions) on Wiley Online Library for rules of use; OA articles are governed by the applicable Creative Commons License

Collectively, our results demonstrated a clear relationship between water depth and SM characteristics with *SVF*. The quantification of *SVF* from field data is consistent with the observed variation in suspended sediment flux, confirming the sediment trapping ability of inundated SM. Additionally, we demonstrated that the combination of low *TKE* and high SVF at the edge of densely vegetated areas promotes significant localized sedimentation. The newly deposited coarser substrate, creates a favorable environment for SM seedlings to establish and develop their underground root systems (Gill & Tomlinson, 1977; Lovelock et al., 2006). Once established, young SMs at the fringe further enhance sediment retention and, with sufficient sediment supply, promote vertical accretion and further vegetation progradation toward the offshore area, thereby expanding the intertidal zone (D'Alpaos, 2011; Krauss et al., 2014; Tognin et al., 2025). Healthy mangroves contribute to sedimentation rates of approximately 1–8 mm/yr, generally exceeding local mean sea-level rise rates (Gilman et al., 2008; Horstman et al., 2014). The seaward expansion of SMs, facilitated by abundant and heterogeneous sediment supply, potentially increases mangrove patch coverage. The vertical accretion and horizontal expansion of SMs enhance mangrove shoreline resilience to sea-level rise. Our study focuses on SM transects primarily influenced by tidal dynamics and seaward sediment transport, with minimal input from upstream sources. Additionally, the study area is sheltered by adjacent islands, contributing to a relatively stable hydrodynamic environment. In contrast, when sediment supply is insufficient to keep pace with sea-level rise, this biologically induced positive feedback does not occur, and vegetation is no longer effective in mitigating the effects of rising sea level. Under these conditions, abiotic factors tend to play a dominant role in shaping the retreating intertidal morphology. To gain deeper insights into mangrove shoreline changes, it is essential to assess how different species respond to sediment-starved environmental conditions.

5. Conclusions and Outlook

Shrub mangroves, which commonly grow in subtropical tidal flats, are typically less than 1.5 m tall and exhibit a wider-angled canopy structure than tree mangroves. Given the constraints on coastal land use due to anthropogenic activities, the natural accretion of mangrove tidal flats may offer a viable ecological solution to challenges posed by rising sea levels. In this study, hydrodynamic and sediment transport data were collected during a spring-neap tidal cycle (from 9 to 14 October 2021) from a tidal flat colonized by SMs. To quantify the submerged fraction of vegetation as a function of local water depth, which strongly influences flow energy dissipation, we used the submerged volume fraction (*SVF*) metric. The data indicate minimal spatial variation in water depth along the transect. However, in the sparsely vegetated seaward section of the transect, the average flow velocity and SSC were 0.16 $m{\cdot}s^{-1}$ and 1.75 $kg{\cdot}m^{-3}$, respectively. In contrast, in the more densely vegetated landward section, these values decreased to 0.07 $m{\cdot}s^{-1}$ and 0.26 $kg{\cdot}m^{-3}$, respectively. At the edge of the dense mangrove patch, where plant density increases significantly moving landward, reduced *TKE* and increased *SVF* likely explain the observed sediment coarsening shift. Surface sediment grain size data collected 1 year apart (January and November 2021) at the leading edge of the dense mangrove patch show a decrease in clay content and an increase in silt content, leading to a coarser surface bed composition. This coarser sediment creates a more favorable environment for the growth of mangrove seedlings. These findings suggest that SMs have the ability to modify local hydrodynamic and sedimentary conditions, promoting bed elevation accretion at the margin of the vegetated flat. This process establishes a positive feedback loop, allowing the mangrove seaward expansion with abundant and heterogeneous sediment supply, potentially gaining more coverage area of mangrove patch. SMs' vertical accretion and horizontal expansion enhance mangrove shoreline resilience to sea-level rise.

Conflict of Interest

The authors declare no conflicts of interest relevant to this study.

Data Availability Statement

The field measurement data at an SM tidal flat in China, which contains the hydrodynamic data, vegetation data, and sedimentary data are available at Zhou (2025) (Research data Unipd) via https://researchdata.cab.unipd.it/id/eprint/1635 with creative commons—Attribution 4.0 license.

21698961, 2025, 10, Downloaded from https://agupubs.onlinelibrary.wiley.com/doi/10.1029/2025JG008765 by Zhijun Dai - East China Normal University , Wiley Online Library on [24/10/2025]. See the Terms and Conditions (https://onlinelibrary.wiley.com/terms-and-conditions) on Wiley Online Library for rules of use; OA articles are governed by the applicable Creative Commons License

Acknowledgments
This study was financially supported by the National Key R&D Program of China (2023YFE0121200), the National Natural Science Foundation of China (41930537, 42366009, and 42366008), Shanghai International Science and Technology Cooperation Fund Project (23230713800), and the PRIN project, "Reconciling coastal flooding protection and morphological conservation of shallow coastal environments" via the Italian Ministry for University and Research (Grant Number 2022FZNH82).

References

Adame, M. F., Reef, R., Santini, N. S., Najera, E., Turschwell, M. P., Hayes, M. A., et al. (2021). Mangroves in arid regions: Ecology, threats, and opportunities. *Estuarine, Coastal and Shelf Science*, *248*, 106796. https://doi.org/10.1016/j.ecss.2020.106796

Anton, A., Almahasheer, H., Delgado, A., Garcias-Bonet, N., Carrillo-de-Albornoz, P., Marbà, N., et al. (2020). Stunted mangrove trees in the oligotrophic central Red Sea relate to nitrogen limitation. *Frontiers in Marine Science*, *7*, 597. https://doi.org/10.3389/fmars.2020.00597

Bechtold, B. (2016). Violin plots for Matlab, Github project. Retrieved from https://github.com/bastibe/Violinplot-Matlab

Besset, M., Gratiot, N., Anthony, E. J., Bouchette, F., Goichot, M., & Marchesiello, P. (2019). Mangroves and shoreline erosion in the Mekong River delta, Viet Nam. *Estuarine, Coastal and Shelf Science*, *226*, 106263. https://doi.org/10.1016/j.ecss.2019.106263

Bird, E. C. F. (1986). Mangroves and intertidal morphology in Westernport bay, Victoria, Australia. *Marine Geology*, *69*(3–4), 251–271. https://doi.org/10.1016/0025-3227(86)90042-3

Carniello, L., D'Alpaos, A., Botter, G., & Rinaldo, A. (2016). Statistical characterization of spatio-temporal sediment dynamics in the Venice lagoon. *J. Geophys. Res.Earth Surface*, *121*(5), 1049–1064. https://doi.org/10.1002/2015JF003793

Cheng, N. S., Wei, M. X., Chiew, Y. M., Lu, Y. S., & Emadzadeh, A. (2020). Combined effects of mean flow and turbulence on sediment pickup rate. *Water Resources Research*, *56*(2), e2019WR026181. https://doi.org/10.1029/2019WR026181

Cintrón, G., Lugo, A. E., Pool, D. J., & Morris, G. (1978). Mangroves of arid environments in Puerto Rico and adjacent islands. *Biotropica*, *10*(2), 110–121. https://doi.org/10.2307/2388013

Cintrón, G., & Schaeffer Novelli, Y. (1984). Methods for studying mangrove structure. *Monographs on Oceanographic Methodology*, *8*, 91–113.

Committee of Annals of Chinese Estuaries. (1998). *Annals of Chinese estuaries* (Vol. 14). Ocean Press.

D'Alpaos, A. (2011). The mutual influence of biotic and abiotic components on the long-term ecomorphodynamic evolution of salt-marsh ecosystems. *Geomorphology*, *126*(3–4), 269–278. https://doi.org/10.1016/j.geomorph.2010.04.027

Ellison, J. C. (2009). Geomorphology and sedimentology of mangrove swamps. In G. M. E. Perillo, E. Wolanski, D. Cahoon, & M. Brinson (Eds.), Coastal Wetlands*: An ecosystem integrated approach* (pp. 564–591). Elsevier Science.

Ellison, J. C. (2019). Biogeomorphology of mangroves. In *Coastal wetlands* (pp. 687–715). Elsevier.

Feller, I. C. (1995). Effects of nutrient enrichment on growth and herbivory of dwarf red mangrove (Rhizophora mangle). *Ecological Monographs*, *65*(4), 477–505. https://doi.org/10.2307/2963499

Feller, I. C., McKee, K. L., Whigham, D. F., & O'neill, J. P. (2003). Nitrogen vs. phosphorus limitation across an ecotonal gradient in a mangrove forest. *Biogeochemistry*, *62*(2), 145–175. https://doi.org/10.1023/A:1021166010892

Folk, R. L., & Ward, W. C. (1957). Brazos River bar [Texas]; a study in the significance of grain size parameters. *Journal of Sedimentary Research*, *27*(1), 3–26. https://doi.org/10.1306/74D70646-2B21-11D7-8648000102C1865D

Friess, D. A., Krauss, K. W., Horstman, E. M., Balke, T., Bouma, T. J., Galli, D., & Webb, E. L. (2012). Are all intertidal wetlands naturally created equal? Bottlenecks, thresholds and knowledge gaps to mangrove and saltmarsh ecosystems. *Biological Reviews*, *87*(2), 346–366. https://doi.org/10.1111/j.1469-185X.2011.00198.x

Gajre, R. B., Rahman, M. S., Ghosh, T., & Friess, D. A. (2024). Variations in biophysical characteristics mangroves along retreating and advancing shorelines. *Science of The Total Environment*, *926*, 171690. https://doi.org/10.1016/j.scitotenv.2024.171690

Gill, A. M., & Tomlinson, P. B. (1977). Studies on the growth of Red Mangrove (Rhizophora mangle L.) 4. The adult root System. *Biotropica*, *9*(3), 145–155. https://doi.org/10.2307/2387877

Gilman, E. L., Ellison, J., Duke, N. C., & Field, C. (2008). Threats to mangroves from climate change and adaptation options: A review. *Aquatic Botany*, *89*(2), 237–250. https://doi.org/10.1016/j.aquabot.2007.12.009

Glover, H. E., Stokes, D. J., Ogston, A. S., Bryan, K. R., & Pilditch, C. A. (2022). Decadal-scale impacts of changing mangrove extent on hydrodynamics and sediment transport in a quiescent, mesotidal estuary. *Earth Surface Processes and Landforms*, *47*(5), 1287–1303. https://doi.org/10.1002/esp.5317

Goring, D. G., & Nikora, V. I. (2002). Despiking acoustic Doppler velocimeter data. *Journal of Hydraulic Engineering*, *128*(1), 117–126. https://doi.org/10.1061/(ASCE)0733-9429(2002)128:1(117)

Horstman, E. M., Dohmen-Janssen, C. M., Bouma, T. J., & Hulscher, S. J. M. H. (2015). Tidal-scale flow routing and sedimentation in mangrove forests: Combining field data and numerical modelling. *Geomorphology*, *228*, 244–262. https://doi.org/10.1016/j.geomorph.2014.08.011

Horstman, E. M., Dohmen-Janssen, C. M., Narra, P. M. F., Van den Berg, N. J. F., Siemerink, M., & Hulscher, S. J. (2014). Wave attenuation in mangroves: A quantitative approach to field observations. *Coastal Engineering*, *94*, 47–62. https://doi.org/10.1016/j.coastaleng.2014.08.005

Jennerjahn, T. C., Gilman, E., Krauss, K. W., Lacerda, L. D., Nordhaus, I., & Wolanski, E. (2017). Mangrove Ecosystems under climate change. In V. H. Rivera-Monroy, S. Y. Lee, E. Kristensen, & R. R. Twilley (Eds.), *Mangrove ecosystems: A global biogeographic perspective* (pp. 211–244). Springer.

Kauffman, J. B., & Donato, D. C. (2012). *Protocols for the measurement, monitoring and reporting of structure, biomass and carbon stocks in mangrove forests* (Vol. 86). Cifor.

Kozlowski, T. T. (1999). Soil compaction and growth of woody plants. *Scandinavian Journal of Forest Research*, *14*(6), 596–619. https://doi.org/10.1080/02827589908540825

Krauss, K. W., Allen, J. A., & Cahoon, D. R. (2003). Differential rates of vertical accretion and elevation change among aerial root types in Micronesian mangrove forests. *Estuarine, Coastal and Shelf Science*, *56*(2), 251–259. https://doi.org/10.1016/S0272-7714(02)00184-1

Krauss, K. W., McKee, K. L., Lovelock, C. E., Cahoon, D. R., Saintilan, N., Reef, R., & Chen, L. (2014). How mangrove forests adjust to rising sea level. *New Phytologist*, *202*(1), 19–34. https://doi.org/10.1111/nph.12605

Long, C., Dai, Z., Wang, R., Lou, Y., Zhou, X., Li, S., & Nie, Y. (2022). Dynamic changes in mangroves of the largest delta in northern Beibu Gulf, China: Reasons and causes. *Forest Ecology and Management*, *504*, 119855. https://doi.org/10.1016/j.foreco.2021.119855

Lovelock, C. E., Ball, M. C., Choat, B., Engelbrecht, B. M., Holbrook, N. M., & Feller, I. C. (2006). Linking physiological processes with mangrove forest structure: Phosphorus deficiency limits canopy development, hydraulic conductivity and photosynthetic carbon gain in dwarf Rhizophora mangle. *Plant, Cell and Environment*, *29*(5), 793–802. https://doi.org/10.1111/j.1365-3040.2005.01446.x

Lugo, A. E. (1989). Fringe wetlands. In A. E. Lugo, M. Brinson, & S. Brown (Eds.), *Forested wetlands: Ecosystems of the world 15* (pp. 143–169). Elsevier.

Lugo, A. E., & Snedaker, S. C. (1974). The ecology of mangroves. *Annual Review of Ecology and Systematics*, 39–64. https://www.jstor.org/stable/2096879

Maza, M., Lara, J. L., & Losada, I. J. (2019). Experimental analysis of wave attenuation and drag forces in a realistic fringe Rhizophora mangrove forest. *Advances in Water Resources*, *131*, 103376. https://doi.org/10.1016/j.advwatres.2019.07.006

Montgomery, J. M., Bryan, K. R., Mullarney, J. C., & Horstman, E. M. (2019). Attenuation of storm surges by coastal mangroves. *Geophysical Research Letters*, *46*(5), 2680–2689. https://doi.org/10.1029/2018GL081636

21698961, 2025, 10, Downloaded from https://agupubs.onlinelibrary.wiley.com/doi/10.1029/2025JG008765 by Zhijun Dai - East China Normal University , Wiley Online Library on [24/10/2025]. See the Terms and Conditions (https://onlinelibrary.wiley.com/terms-and-conditions) on Wiley Online Library for rules of use; OA articles are governed by the applicable Creative Commons License

Mullarney, J. C., Henderson, S. M., Norris, B. K., Bryan, K. R., Fricke, A. T., Sandwell, D. R., & Culling, D. P. (2017). A question of Scale: How turbulence around aerial roots shapes the seabed morphology in mangrove forests of the mekong Delta. *Oceanography*, *30*(3), 34–47. https://doi.org/10.5670/oceanog.2017.312

Nguyen, T. P., & Parnell, K. E. (2017). Gradual expansion of mangrove areas as an ecological solution for stabilizing a severely eroded mangrove dominated muddy coast. *Ecological Engineering*, *107*, 239–243. https://doi.org/10.1016/j.ecoleng.2017.07.038

Norris, B. K., Mullarney, J. C., Bryan, K. R., & Henderson, S. M. (2019). Turbulence within natural mangrove pneumatophore canopies. *Journal of Geophysical Research: Oceans*, *124*(4), 2263–2288. https://doi.org/10.1029/2018JC014562

Peng, Y. L., Wang, Y. S., & Gu, J. D. (2015). Identification of suitable reference genes in mangrove Aegiceras corniculatum under abiotic stresses. *Ecotoxicology*, *24*(7–8), 1714–1721. https://doi.org/10.1007/s10646-015-1487-8

Pereira, D. (2025). Wind Rose. MATLAB Central File Exchange. Retrieved from https://www.mathworks.com/matlabcentral/fileexchange/47248-wind-rose

Reef, R., Feller, I. C., & Lovelock, C. E. (2010). Nutrition of mangroves. *Tree Physiology*, *30*(9), 1148–1160. https://doi.org/10.1093/treephys/tpq048

Rusello, P. J., Lohrmann, A., Siegel, E., & Maddux, T. (2006). Improvements in acoustic doppler velocimetery. paper presented at The 7th Int. ICHE, Philadelphia, USA. In *Conf. on hydroscience and engineering*.

Simard, M., Fatoyinbo, L., Smetanka, C., Rivera-Monroy, V. H., Castañeda-Moya, E., Thomas, N., & Van der Stocken, T. (2019). Mangrove canopy height globally related to precipitation, temperature and cyclone frequency. *Nature Geoscience*, *12*(1), 40–45. https://doi.org/10.1038/s41561-018-0279-1

Swales, A., Bentley Sr, S. J., & Lovelock, C. E. (2015). Mangrove-forest evolution in a sediment-rich estuarine system: Opportunists or agents of geomorphic change? *Earth Surface Processes and Landforms*, *40*(12), 1672–1687. https://doi.org/10.1002/esp.3759

Temmerman, S., Horstman, E. M., Krauss, K. W., Mullarney, J. C., Pelckmans, I., & Schoutens, K. (2023). Marshes and mangroves as nature-based coastal storm buffers. *Annual Review of Marine Science*, *15*(1), 95–118. https://doi.org/10.1146/annurev-marine-040422-092951

Tinoco, R. O., & Coco, G. (2016). A laboratory study on sediment resuspension within arrays of rigid cylinders. *Advances in Water Resources*, *92*, 1–9. https://doi.org/10.1016/j.advwatres.2016.04.003

Tognin, D., D'Alpaos, A., Ghinassi, M., & Carniello, L. (2025). Marsh topography reveals the signature of storm-surge-driven sedimentation. *Geology*, *53*(1), 45–49. https://doi.org/10.1130/G52552.1

Tognin, D., Peruzzo, P., De Serio, F., Ben Meftah, M., Carniello, L., Defina, A., & Mossa, M. (2019). Experimental setup and measuring system to study SolitaryWave interaction with rigid emergent vegetation. *Sensors*, *19*(8), 1787. https://doi.org/10.3390/s19081787

Tomiczek, T., Wargula, A., Lomónaco, P., Goodwin, S., Cox, D., Kennedy, A., & Lynett, P. (2020). Physical model investigation of mid-scale mangrove effects on flow hydrodynamics and pressures and loads in the built environment. *Coastal Engineering*, *162*, 103791. https://doi.org/10.1016/j.coastaleng.2020.103791

Ward, R. D., Friess, D. A., Day, R. H., & Mackenzie, R. A. (2016). Impacts of climate change on mangrove ecosystems: A region by region overview. *Ecosystem Health and Sustainability*, *2*(4), e01211. https://doi.org/10.1002/ehs2.1211

Woodroffe, C. (1992). *Mangrove sediments and geomorphology* (Vol. 41, pp. 7–41). Tropical mangrove ecosystems. https://doi.org/10.1029/CE041p0007

Woodroffe, C. D., Rogers, K., McKee, K. L., Lovelock, C. E., Mendelssohn, I. A., & Saintilan, N. (2016). Mangrove sedimentation and response to relative sea-level rise. *Annual Review of Marine Science*, *8*(1), 243–266. https://doi.org/10.1146/annurev-marine-122414-034025

Xu, Y., Li, D., & Nepf, H. (2022). Sediment pickup rate in bare and vegetated channels. *Geophysical Research Letters*, *49*(21), e2022GL101279. https://doi.org/10.1029/2022GL101279

Yoshikai, M., Nakamura, T., Bautista, D. M., Herrera, E. C., Baloloy, A., Suwa, R., et al. (2022). Field measurement and prediction of drag in a planted Rhizophora mangrove forest. *Journal of Geophysical Research: Oceans*, *127*(11), e2021JC018320. https://doi.org/10.1029/2021JC018320

Zhou, X. (2025). Dataset_Shrub mangroves facilitate self-sustaining conditions for colonization: Insights from the Nanliu Delta, China *[Dataset]*. https://doi.org/10.25430/researchdata.cab.unipd.it.00001473

Zhou, X., Dai, Z., Carniello, L., Long, C., Wang, R., Luo, J., & Huang, Z. (2022). Linkage between mangrove wetland dynamics and wave attenuation during a storm–a case study of the Nanliu Delta, China. *Marine Geology*, *454*, 106946. https://doi.org/10.1016/j.margeo.2022.106946

21698961, 2025, 10, Downloaded from https://agupubs.onlinelibrary.wiley.com/doi/10.1029/2025JG008765 by Zhijun Dai - East China Normal University , Wiley Online Library on [24/10/2025]. See the Terms and Conditions (https://onlinelibrary.wiley.com/terms-and-conditions) on Wiley Online Library for rules of use; OA articles are governed by the applicable Creative Commons License